CORA Cork Open Research Archive
Cartlann Taighde Oscailte Chorcaí

Title	Polarimetry analysis and optical contrast of Sb_2S_3 phase change material
Authors	Gutiérrez, Yael;Fernández-Pérez, Andrea;Rosales, Saúl A.;Cobianu, Cornel;Gheorghe, Marin;Modreanu, Mircea;Saiz, José M.;Moreno, Fernando;Losurdo, Maria
Publication date	2022-03-16
Original Citation	Gutiérrez, Y., Fernández-Pérez, A., Rosales, S. A., Cobianu, C., Gheorghe, M., Modreanu, M., Saiz, J. M., Moreno, F. and Losurdo, M. (2022) 'Polarimetry analysis and optical contrast of Sb_2S_3 phase change material', Optical Materials Express, 12(4), pp. 1531-1541. doi: 10.1364/OME.450781
Type of publication	Article (peer-reviewed)
Link to publisher's version	10.1364/OME.450781
Rights	© 2022, Optical Society of America under the terms of the OSA Open Access Publishing Agreement.
Download date	2026-10-30 23:22:57
Item downloaded from	https://hdl.handle.net/10468/12943

UCC
University College Cork, Ireland
Coláiste na hOllscoile Corcaigh

Research Article Vol. 12, No. 4 / 1 Apr 2022 / Optical Materials Express 1531
Optical Materials EXPRESS

Polarimetry analysis and optical contrast of Sb_2S_3 phase change material

Yael Gutiérrez,[1,*] Andrea Fernández-Pérez,[2] Saúl A. Rosales,[2] Cornel Cobianu,[3,4] Marin Gheorghe,[3] Mircea Modreanu,[5] José M. Saiz,[2] Fernando Moreno,[2] and Maria Losurdo[1]

[1]*Institute of Nanotechnology, CNR-NANOTEC, via Orabona 4, 70126 Bari, Italy*
[2]*Department of Applied Physics, Universidad de Cantabria, Avda. Los Castros s/n 39005 Santander, Spain*
[3]*NANOM MEMS, G. Cosbuc 9, 505400 Rasnov, Romania*
[4]*Academy of Romanian Scientists, Science and Information Technology Section, Str. Ilfov Nr. 3, Sector 5, Bucharest, Romania*
[5]*Tyndall National Institute, University College Cork, T12 R5CP Cork, Ireland*
[*]*yael.gutierrezvela@nanotec.cnr.it*

Abstract: Phase-change materials (PCMs) are the cornerstone for the development of reconfigurable and programmable photonic devices. Sb_2S_3 has been recently proposed as an interesting PCM due to its low-losses in the visible and near-IR. Here, we report the use of imaging polarimetry and spectroscopic ellipsometry to reveal and directly measure the optical properties of Sb_2S_3 both in crystalline and amorphous states obtained upon crystallization by annealing in the air of chemical bath deposited amorphous Sb_2S_3. The Mueller Matrix polarimetric analysis reveals the strong anisotropy of the Sb_2S_3 crystallites which crystallize in radial spherulitic domains in contrast to the optical isotropy of the amorphous films. A refractive index contrast of $\Delta n = 0.5$ is demonstrated while maintaining low-losses at telecommunications C-band, i.e., $\lambda = 1550$ nm.

© 2022 Optica Publishing Group under the terms of the Optica Open Access Publishing Agreement

1. Introduction

Phase-change materials (PCMs) can undergo fast and reversible changes between two or more stable crystalline phases with different optical and electrical properties. The contrast in optoelectronic properties between phases is the key feature for the development of a new generation of reconfigurable integrated photonic platforms with application in programmable photonic processing [1], non-volatile memories [2,3] and neuromorphic computing [4], as well as tunable nanophotonic metasurfaces and flat optics with active amplitude/phase control [5,6].

All the former applications have been demonstrated using prototypical $Ge_2Sb_2Te_5$ (GST) as PCM. This material combines switching times in the sub-nanosecond scale reproducible for billions of cycles, low transition temperature (melting temperature $T_m \approx 600$°C and crystallization temperature $T_c \approx 170$°C) and large optical and electrical contrasts (with difference between refractive indices of the amorphous and crystalline phases $\Delta n = 3.56$ and $\Delta k = 1.37$ at telecom wavelengths; and difference in the resistivity of $\Delta\rho > 10^3 \Omega$·m). Nevertheless, while new successful developments in the field of reconfigurable photonics using GST are pursued, other PCMs are being sought to reduce losses in the visible and near-IR spectral ranges. Ideally, a PCM should have a large change in the refractive index to achieve a high modulation in the active spectral region while keeping a low extinction coefficient to prevent energy loss [5].

In chalcogenide materials, it is known that as the chalcogen element decreases in atomic number (i.e. Te → Se → S), the bandgap of the material tends to increase (e.g. band gap energies of Sb_2Te_3, Sb_2Se_3 and Sb_2S_3 are 0.2, 1.2 and 2.1 eV respectively [7–9]) as well as their air stability [10]. Therefore, recent research on PCM materials has focused on light chalcogenides.

#450781 https://doi.org/10.1364/OME.450781
Journal © 2022 Received 7 Dec 2021; revised 24 Jan 2022; accepted 24 Jan 2022; published 16 Mar 2022

Optical Materials EXPRESS

Recently, the performance and capabilities of Sb_2S_3 as PCM has been demonstrated by Dong et al. [7]. Delaney et al. [11], performed over 2000 switching events on Sb_2S_3, while showing not full reproducibility between events. These studies so far have shown a decay in reflection change at all points in the durability cycle, with a drop from 5% to 1% seen over the first 2000 cycles. Reported energy band gaps for amorphous and crystalline Sb_2S_3 are 2.05 and 1.72 eV as opposed to the 0.5 and 0.7 eV reported for amorphous and crystalline GST [7]. Sb_2S_3 has low melting and crystallization temperatures ($T_m \approx 550$°C and crystallization temperature T_c

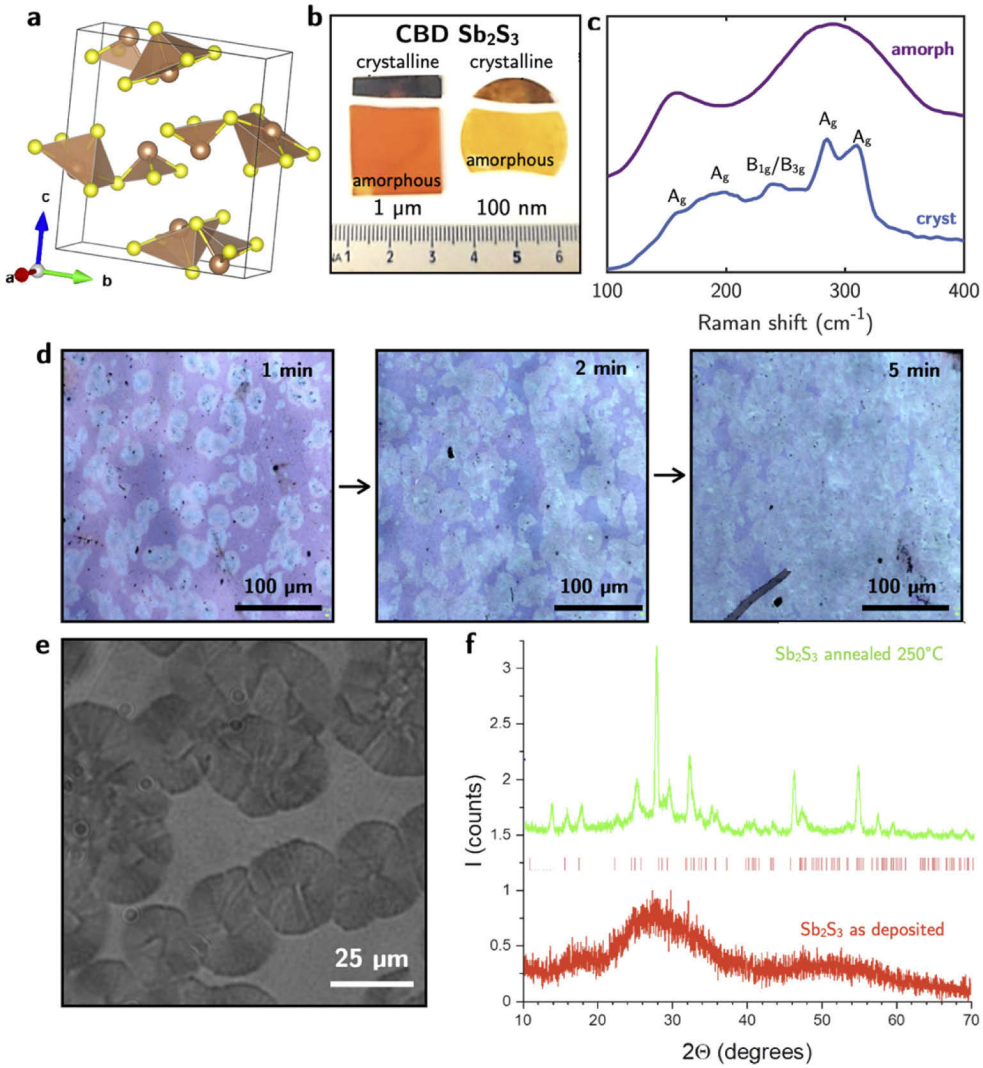


Fig. 1. (a) Unit cell of crystalline Sb_2S_3. Sb and S atoms are represented in brown and tallow respectively. (b) Photograph of the as grown and thermally crystallized Sb_2S_3 film of thickness of approximately 100 nm and 1 µm. (c) Raman spectra of the as grown amorphous and thermally crystallized Sb_2S_3. (d, e) Micrographs of the crystallization process evolution taken on the 100 nm film (after 1 min, 2 min and 5 min of annealing) from the formation of initial seed crystals on the amorphous material to complete crystallization of the sample. (f) X-ray diffraction pattern of as-deposited 100 nm Sb_2S_3 film and annealed at 250°C. Vertical red lines indicate the Bragg position of Sb_2S_3.

Optical Materials EXPRESS

≈ 250°C). Sb_2S_3 crystallizes in an orthorhombic structure with space group symmetry *Pnma* (no. 62) with lattice parameters $a = 1.1302$ nm, $b = 0.3834$ nm, and $c = 1.1222$ nm with excellent cleavage on (100) and crystals commonly elongated along the *b* axis. Interestingly, Sb_2S_3 is a layered materials with van der Waals interaction between chalcogenides (sulphur) planes as shown in Fig. 1(a). Sb_2S_3 is a biaxial anisotropic material, and optical constants were measured at specific wavelengths many years ago on natural cleavage surfaces, i.e., along axes *b* and *c*, by Tyndall [12] and Drude [13]. Recently, Schübert et al. [14,15] reported the complete dielectric function tensor. Nevertheless, while single crystals and bidimensional (2D) layers of Sb_2S_3 are birefringent, thermal annealed Sb_2S_3 are polycrystalline consisting of a texture of micron-sized crystalline domains for which it is still an open question their degree of anisotropy and how this can affect the performance of the optical devices. In this context, imaging Mueller Matrix (MM) polarimetric analysis in combination with optical microscopy becomes a key technique to analyze the optical behavior of microtextured biaxial anisotropic thin film samples [16].

In this work, imaging polarimetry is used to study the optical properties of amorphous chemical bath deposited Sb_2S_3 thin films as well as of thermally annealed films. Imaging polarimetry reveals the spherulitic crystallization leading to anisotropic, birefringent, and dichroic Sb_2S_3 micro-crystals in the film. The refractive index spectrum of both the amorphous and thermally crystallized phases is reported as well as the refractive index contrast, i.e., the key parameter for the benchmarking of this material as PCM.

2. Methods

2.1. Film fabrication

Sb_2S_3 films were deposited by chemical bath deposition (CBD) [17] at 15°C using antimony chloride ($SbCl_3$) and sodium thiosulfate as precursors. At that temperature, a $SbCl_3$ was dissolved in 4 mL of methanol (0.35 M solution) and 1.1 g of $Na_2S_2O_3$ was dissolved in 25 mL of deionized (DI) water (0.28 M solution). These two solutions were mixed, and then DI water was added to obtain a total volume of 50 ml of the liquid phase, which had a pH equal to 4. The final mixture was vigorously stirred for 5 minutes. The glass substrates were cleaned in 5% sodium hydroxide at 90°C followed by 1N HCl, and absolute ethanol. After rinsing in DI water, the glass slides were dried at 80°C and then immersed in a vertical position in a beaker. The growth time was between 2 h - 4 h to have a film thickness in the range 100 nm to 1 µm.

2.2. Structural characterization

Raman spectroscopy was performed in with LabRam Horiba set up using a ×100 microscope objective (NA = 0.9) and excitation wavelength of 633 nm allowing us to monitor the structural changes induced by the thermal crystallization.

The crystalline structure was determined by X-ray diffraction, in thin film geometry. The measurements were performed with an Ultima IV diffractometer (Rigaku Corp., Japan), equipped with parallel beam optics and a thin film attachment, using Cu Kα radiation ($\lambda = 1.5405$ Å), operated at 30 mA and 40 kV, over the 2θ range 5-70°, at a scanning rate of 1°/min, with a step width of 0.02°; the fixed incidence angle was set at 0.5°. Phase identification was performed using Rigaku's PDXL software, connected to the ICDD PDF-2 database. The lattice constants were refined using diffraction line position and the crystallite size was estimated from the diffraction line width (full width at half maximum, FWHM) using the Scherrer equation.

2.3. Optical characterization

For statistical analysis of the optical properties, amorphous and spherulitic crystallized samples were measured in 5 points on two different batches of samples of thickness 100 nm following the same deposition and subsequent crystallization process.

Optical Materials EXPRESS

Optical properties, namely spectra of the complex pseudodielectric function, $\langle\varepsilon\rangle = \langle\varepsilon_1\rangle + i\langle\varepsilon_2\rangle$, were measured by spectroscopic ellipsometry (UVISEL Horiba) in the photon energy range 0.75–6.5 eV with a resolution of 0.05 eV. In order to check anisotropy of samples, measurements at various angle of incidence in the range 55°-75° were performed indicating that the films were mostly isotropic. The ellipsometric measurements were fit to a three-media substrate/film/air model, where the glass substrate was experimentally measured prior deposition; the Sb_2S_3 layer was parameterized using the Tauc–Lorentz oscillators model [18].

Spectral transmittance measurements were performed with a microscope set-up (Nikon Eclipse-NiU) where the sample, located in the sample holder, was illuminated by an aplanatic achromatic condenser lens (variable NA1.4) and the transmitted light collected by an optical system consisting of an objective (Nikon, infinity corrected, NA0.45) and a focusing lens to concentrate the transmitted light at the entrance of an optical fiber (NA0.22). This guides the light to a spectrograph (ANDOR SR3031A) with a CCD camera (ANDOR DV420A-OE) which is controlled by a PC. The camera signal, previously corrected by the spectra of the illuminating lamp, is suitably analyzed to get the desired spectral data.

Polarimetric measurements were performed by an imaging polarimeter that allowed measuring the Mueller Matrices (MM) at different wavelengths in the visible spectrum. The instrument used in the experiment is a dynamic rotating compensator polarimeter. It consisted of a Polarization State Generator (PSG) composed of a Polarizer (P1) and a λ/4 waveplate Retarder (R1), a sample holder, a 5× Microscope Objective (MO) with a numerical aperture of 0.15 aligned in the transmission configuration, which allowed studying the sample in the microscopic range, and a Polarizer State Analyzer (PSA), which in turn was composed of another λ/4 waveplate retarder (R2) and an analyzer (P2). The microscope objective was interchangeable so that measurements with different magnifications were possible. Finally, the images were captured with a 12-bit camera. Both retarders rotated synchronously with a speed ratio of 5/2, completing a full Fourier measurement cycle of 200 images of 640×640 pixels with which the low noise MM was calculated by means of a Fourier transformation algorithm [19]. Retarder R1 rotated in angular steps of $2\pi/200$ rad. In total, the full process of one measurement required 10 min. The light source was a supercontinuum laser (FemtoPower 1060 made by Fianium), which allowed performing measurements in the visible spectrum, from 480–680 nm. The wavelength selection was performed by a calibrated diffraction grating and a diaphragm. For the results shown here, the wavelength was centered at $\lambda = 634$ nm with a FWHM = 3 nm, a spectral width high enough to lose coherency and avoid a speckle pattern.

The differential representations of an optical medium are useful in determining the optical properties from measurements [20]. Here, we perform a differential analysis of the Mueller matrices using the Mueller Matrix Differential Decomposition (MMDD). The differential matrix $\boldsymbol{m}$ relates the Mueller matrix $\boldsymbol{M}$ as

$$\frac{d\boldsymbol{M}}{dz} = \boldsymbol{m}\boldsymbol{M} \tag{1}$$

If the differential matrix, $\boldsymbol{m}$ does not depend on z, i.e., distance travelled along the direction of propagation, the solution of this differential equation is found by taking the logarithm of $\boldsymbol{M}$, thus,

$$\boldsymbol{m} = ln(\boldsymbol{M}) \tag{2}$$

The most general form of the differential Mueller matrix for a non-depolarizing medium is given as follows [20–22]

$$\boldsymbol{m} = \begin{pmatrix} \alpha & -LD & -LD' & CD \\ -LD & \alpha & CB & LB' \\ -LD' & -CB & \alpha & -LB \\ CD & -LB' & LB & \alpha \end{pmatrix} \tag{3}$$

Optical Materials EXPRESS

where LD, LD′ and CD are linear dichroism in the *x*-*y* axes, linear dichroism in the 45-135° and circular dichroism. LB, LB′ and CB stand for linear birefringence in the *x*-*y* and 45-135° axes and circular birefringence, respectively. The value α is the absorption coefficient.

The dichroic properties of a medium are due to the anisotropy of its extinction coefficient $\Delta k_{p,q}$ that results in different absorptions for two orthogonal polarization states (*p*,*q*). Conversely, the birefringent properties stem from the anisotropy in the real refractive index $\Delta n_{p,q}$, entailing different phase shifts for two orthogonal polarization states [23]. Therefore, expressions for LD, LD′, CD, LB, LB′ and CB can be written as

$$\begin{aligned} LD &= \tfrac{2\pi}{\lambda}\Delta k_{x-y} & LB &= \tfrac{2\pi}{\lambda}\Delta n_{x-y} \\ LD' &= \tfrac{2\pi}{\lambda}\Delta k_{45°-135°} & LB' &= \tfrac{2\pi}{\lambda}\Delta n_{45°-135°} \\ CD &= \tfrac{2\pi}{\lambda}\Delta k_{L-R} & CB &= \tfrac{2\pi}{\lambda}\Delta n_{L-R} \end{aligned} \tag{4}$$

3. Results

As grown large area CBD Sb_2S_3 samples were annealed for 5 minutes in ambient at 250°C, as shown in Fig. 1(b) in order to ensure a homogenous coverage of crystalline domains. The as-deposited films show a uniform orange color that after annealing turns into dark brownish. Figure 1(c) shows the Raman spectra of the as grown Sb_2S_3 showing two broad peaks characteristic confirming its amorphous state, and further supported by the lack of peaks in the X-ray diffraction (XRD) spectrum in Fig. 1(f). The broad Raman bands at ≈ 140 and 300 cm^{-1} correspond to Sb-S and S = S vibrational modes. After annealing, several peaks appear in the Raman and XRD spectra consistent with Sb_2S_3 crystallites formation. The Raman spectrum of the thermally crystallized Sb_2S_3 shows peaks due to vibrational modes of symmetry groups A_g at 154 cm^{-1} (lattice mode), 190 cm^{-1} (anti-symmetric S–Sb–S bending mode), 285 cm^{-1} (anti- symmetric Sb–S stretching mode), and 308 cm^{-1} (symmetric Sb–S stretching vibration), and B_{1g}/B_{3g} at 241 cm^{-1} (symmetric S–Sb–S bending mode) [24,25]. Fig. 1(d) shows the micrographs of the 100 nm Sb_2S_3 film at different stages of the crystallization process i.e., after 1 min, 2 min and 5 min of annealing. From the first micrograph it can be seen how crystal seeds (blue regions) appear in the amorphous film (purple regions). With increasing annealing time, the crystalline domains grow steadily until covering most of the film and ultimately completing the crystallization of the film. Higher magnification micrographs are shown in Fig. 1(e) where crystalline domains in the amorphous background can be appreciated.

Already the difference in color between the amorphous and crystalline domains in Fig. 1(d) indicates the difference in the refractive index between the two phases. Both the 100 nm and 1 μm amorphous films were measured in the 200-1600 nm range using spectroscopic ellipsometry before and after the thermal crystallization to determine the refractive index, shown in Fig. 2(a). The 100 nm and 1 μm amorphous Sb_2S_3 films have the same refractive index, indicating that the refractive index of the amorphous phase is independent of thickness (the films were deposited under the same experimental conditions; only the deposition time was changed). Interestingly, for the fully crystallized films, the same refractive index was measured for both the 100 nm and the 1 μm both crystallized at same annealing temperature of 250°C. We found that the refractive index, and of course crystallization, depends on the temperature of the annealing rather than on thickness. From the Tauc-Lorentz parameterization of the Sb_2S_3 layer in each sample, the band gap was determined to be 2.10 ± 0.05 and 1.80 ± 0.05 eV for amorphous and crystalline Sb_2S_3, respectively.

These values are in good agreement with those reported by Dong et al. [7], i.e., 2.05 ± 0.05 eV and 1.72 ± 0.05 eV respectively. However, differences in the value of refractive index are observed. For RF sputtered Sb_2S_3 films, the refractive index has been reported to be n = 2.7 and 3.3 at 1550 nm for amorphous and crystalline, respectively, in contrast to the values of n = 1.94 and 2.45

Optical Materials EXPRESS

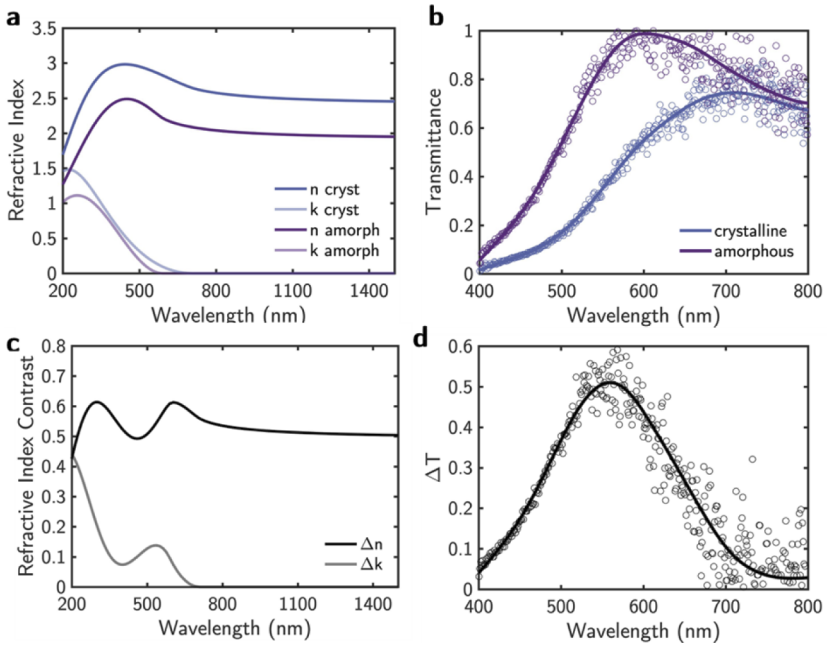


Fig. 2. (a) Refractive index ($n + ik$) of as-grown amorphous and thermally crystalized Sb_2S_3. (b) Transmittance of the as-grown amorphous and thermally crystalized Sb_2S_3. (c) Refractive index contrast Δn and Δk between amorphous and thermally crystalized Sb_2S_3. (d) Difference in the transmittance spectra ΔT measured on the as-grown amorphous and thermally crystalized Sb_2S_3 film.

reported here. These values of refractive index for our CBD Sb_2S_3 films are closer to that reported for electrophoretic deposited Sb_2S_3 films, [26] indicating an effect of the deposition method and parameters on the density of the amorphous Sb_2S_3 film and consequently on the crystallized film density. For reference, at 1550 nm the values of the refractive index tensor measured in a single crystal along the optical axes are $n_a \approx 2.89$, $n_b \approx 3.74$ and $n_c = 3.55$ as reported by Schübert et al. [14]. From the measured values of the refractive indices of the amorphous and crystalline Sb_2S_3 phases, the refractive index contrast is stablished as shown in Fig. 2(b). From 700 to 1600 nm the value of $\Delta n = 0.55$–0.60 while keeping $\Delta k < 10^{-2}$. These values of Δn are comparable to those reported by Delaney et al. [11] (Δn ~0.60 in the 800–1550 nm range) and slightly lower than that reported by Dong et al. [7] ($\Delta n = 1$ at 600 nm) for RF sputtered films. Transmittance measurements performed on both amorphous and thermally crystallized Sb_2S_3 films are shown in Fig. 2(c). The transmittance values for the amorphous films are higher, consistent with its lower refractive index and higher energy band gap. The difference in transmittance ΔT measured between amorphous and thermally crystallized film is shown in Fig. 2(d). A maximum of ΔT as high as 0.5 is reached at 550 nm, indicating that Sb_2S_3 can work as a PCM at optical frequencies.

The imaging Mueller Matrix (MM) was measured in multiple points of two different as-grown amorphous Sb_2S_3 samples of thickness 100 nm showing same optical response. As the MM is measured in transmission, the lower of the fabricated thickness was chosen as it allows us to have the highest signal in the detector minimizing the signal-to-noise ratio. The MM measured on amorphous Sb_2S_3 as shown in Fig. 3. This reveals an almost identity matrix with only non-null elements in the diagonal. From this, and considering the MMDD described above, the linear birefringence (LB), linear dichroism (LD), circular birefringence (CB) and circular dichroism

Optical Materials EXPRESS

(CD) can be obtained as shown in Fig. 4. These parameters show clearly a non-birefringent and non-dichroic behavior characteristic of an isotropic amorphous phase.

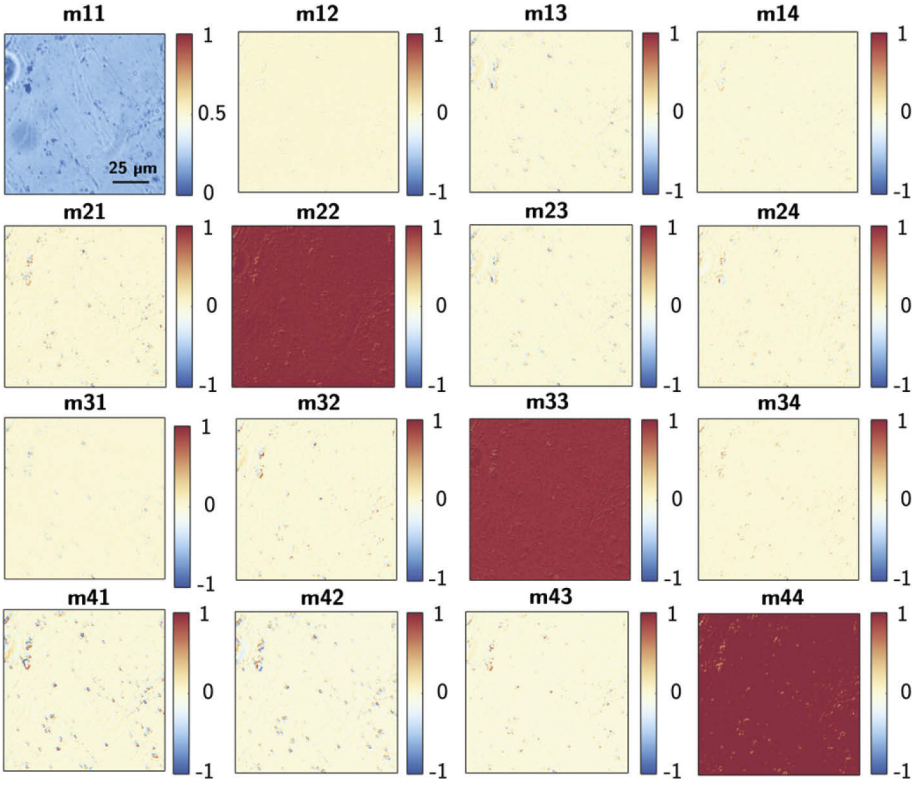


Fig. 3. Experimental Mueller matrix of amorphous Sb_2S_3 films measured at $\lambda = 634$ nm with a 5× microscope objective.

The imaging Mueller Matrix (MM) was also measured after the annealing of the Sb_2S_3 film in crystallized state in which both amorphous and crystalline domains coexist as shown in Fig. 5. Element *m11* represents the micrograph of the studied region. Its morphology consists in round crystalline domains embedded in the amorphous matrix. In this case, and differently from the amorphous Sb_2S_3 in Figs. 3, the MM matrix elements *m24*, *m42*, *m34* and *m43* are non-null in the crystalline domains. As shown in Fig. 6, through the MMDD, the LB, LD, CB and CD parameters can be extracted revealing clearly a birefringent behavior (LB ≠ 0) in the crystalline domains with a slight LD due to the different refractive index and extinction coefficients associated to the dielectric tensor of Sb_2S_3 [14,15], and a lack of optical activity given by the null values of CB and CD.

To better understand those birefringent domains appearing in the film and its relation to crystallization process, cross-polarization measurements on an isolated crystalline domain were performed as shown in Fig. 7. The cross-polarization images present the characteristic Maltese cross pattern (i.e., the four dark perpendicular cones diverging from the center of the crystal). This behavior, characteristic of birefringent materials, is the result of a crystallization process obeying a fast radial growth in a fibrous manner starting from a central seed consistent with spherulitic structures [27]. Generally, the name spherulite is given to radially polycrystalline aggregates with an outer circular/spherical envelope depending of the dimensionality [28]. The spherulitic crystallization of amorphous Sb_2S_3 has already reported in literature when applying similar annealing conditions revealing that the splitting planes (i.e., the boundary between the fibers) not

Optical Materials EXPRESS

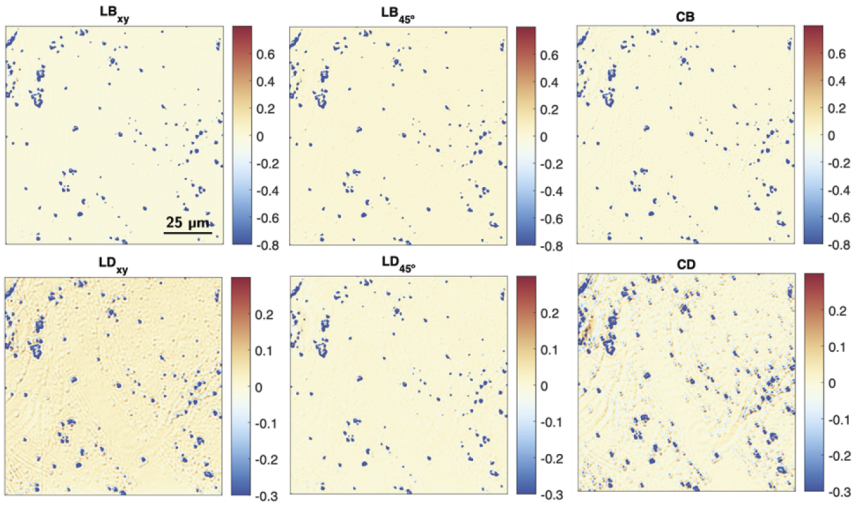


Fig. 4. Mueller Matrix Differential Decomposition of amorphous Sb_2S_3 film measured at $\lambda = 634$ nm. LD, LD′ and CD parameters are linear dichroism in the x-y axes, linear dichroism in the 45-135° and circular dichroism, respectively. LB, LB′ and CB parameters stand for linear birefringence in the x-y and 45-135° axes and circular birefringence, respectively. The blue dots are just dust on the film surface.

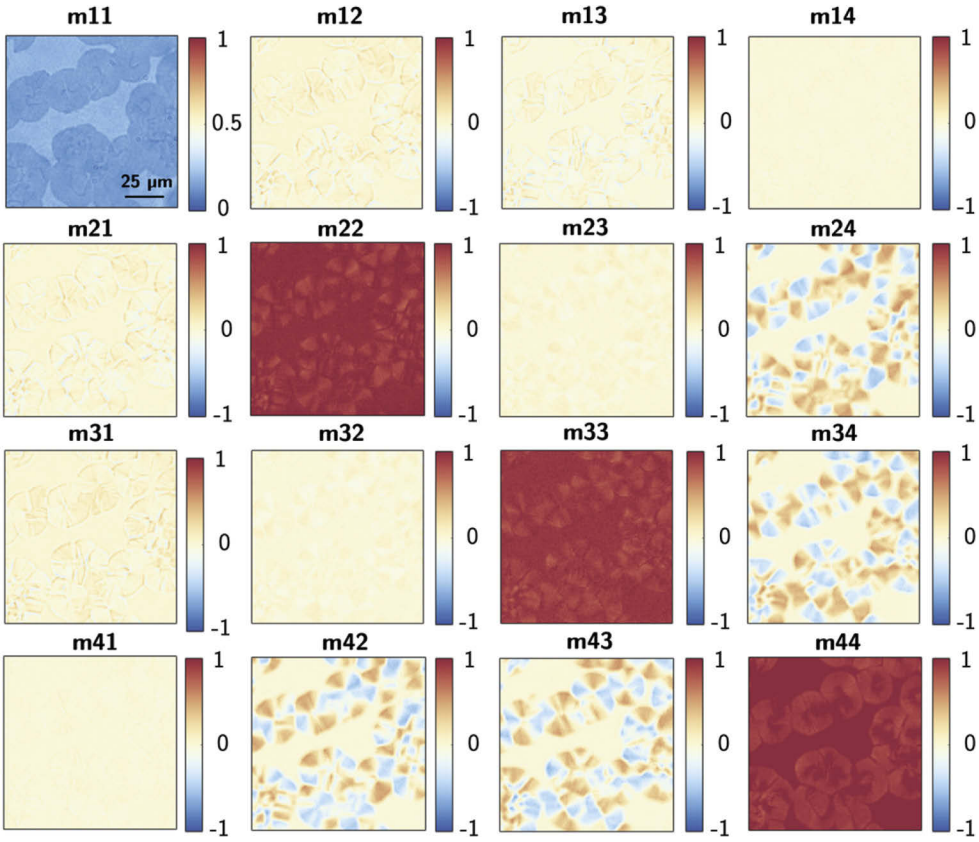


Fig. 5. Experimental Mueller matrix of partially thermally crystallized Sb_2S_3 films measured at $\lambda = 634$ nm with a 5× microscope objective.

Optical Materials EXPRESS

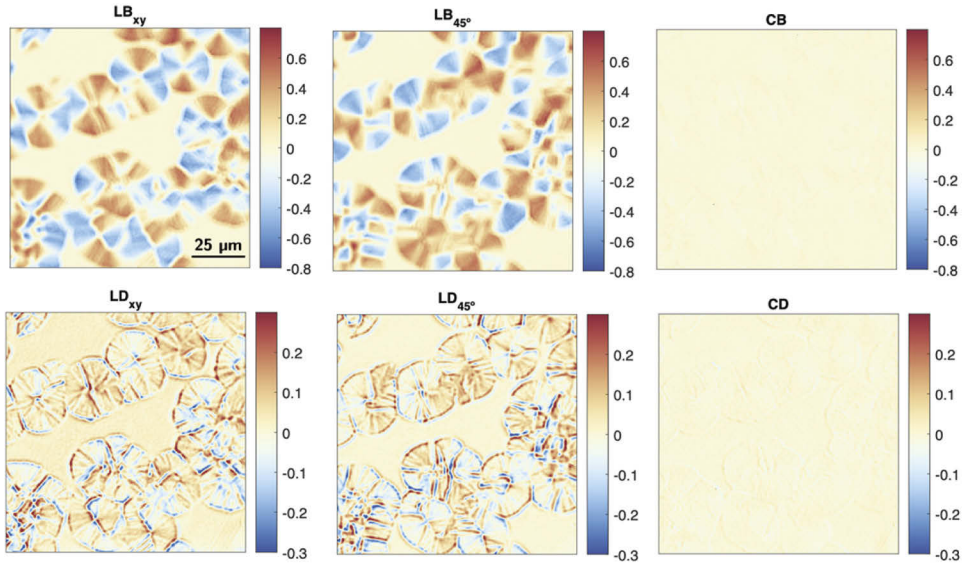


Fig. 6. Mueller Matrix Differential Decomposition of partially thermally crystallized Sb_2S_3 films measured at $\lambda = 634$ nm. LD, LD′ and CD parameters are linear dichroism in the x-y axes, linear dichroism in the 45-135° and circular dichroism, respectively. LB, LB′ and CB parameters stand for linear birefringence in the x-y and 45-135° axes and circular birefringence, respectively.

necessarily coincide with the cleavage planes but only depends on the fastest growth direction [29]. Deep crystallographic analysis using electron microscope crystal lattice imaging techniques was performed by Sokol et al. [30] to study the spherulitic crystallization of amorphous Sb_2S_3. The observation of the Maltese cross pattern signifies only that the anisotropic crystals are arranged in such a way as to conform Fig. 7(c) in which it can be distinguished a radial and tangential refractive index [27] which usually match a crystallographic axis in the case of Sb_2S_3 [29]. Within this context, the Maltese cross pattern can be understood as if each radial fiber in the crystal can be regarded as a linear polarizer. If their direction coincides with that of one of the crossed polarizers, then little light is transmitted. The transmission is increased when the crystalline fibers make a non-zero angle with both polarizers reaching a maximum value when the angle between fiber and polarizers is 45°. Noteworthy, although several Mueller matrix imaging analysis of polycrystalline spherulitic materials have already been reported in literature [31–34], none of them has addressed studies on this type of crystallization on phase-change materials.

Although this spherulitic crystals give a local linear birefringent and dichroic behavior within the micro-crystallite domains, at the macroscopic level, considering full spherulites illuminated with unpolarized white light, the anisotropic behavior with radial symmetry of each spherulite is averaged giving as a result an overall isotropic response also for the crystallized film, consistently with the macroscopic ellipsometric measurement (over mm-size spot). On the contrary, if working with smaller size spots in a way in which only parts of the spherulites are illuminated, because now the radial symmetry lost, linear birefringence and dichroism effects need to be considered. Therefore, the appropriate consideration of isotropy/anisotropy and, thus, the spherulitic growth, is needed for the correct and accurate modelling of the interaction of light with PCMs in phase-change photonic devices.

Optical Materials EXPRESS

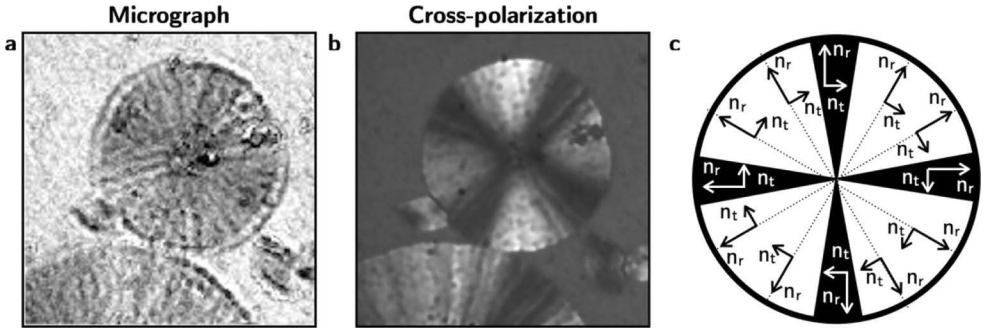


Fig. 7. (a) Micrograph and (b) cross-polarization measured on an isolated crystalline domain. (c) Sketch of the anisotropy in spherulitic structures indicating spatially the radial and tangential refractive indices (n_r and n_t).

4. Conclusions

In this work, we assessed the optical properties of Sb_2S_3 phase-change material using spectroscopic ellipsometry and imaging polarimetry. Amorphous Sb_2S_3 thin films over centimeter scale substrates were prepared by chemical bath deposition and crystallized by thermal annealing in air. Imaging polarimetry reveals the spherulitic crystallization leading to birefringent and dichroic Sb_2S_3 micron-sized crystals, which because of their radial symmetry results in isotropic behavior of crystallized films at macroscopic scale. The refractive index and extinction coefficient spectra of both the amorphous and thermally crystallized phases have been reported as well as the refractive index contrast, which is the key parameter for benchmarking this PCM. A contrast of refractive index of $\Delta n = 0.5$ is demonstrated while the main advantage is maintaining low-losses at telecommunications C-band, i.e., $\lambda = 1550$ nm.

Funding. Horizon 2020 Framework Programme (No 899598 – PHEMTRONICS).

Acknowledgments. S.A.R. and A.F-P thanks the University of Cantabria for his FPU and Augusto González de Linares grants respectively. The authors acknowledge Dr. Alfredo Franco for his assistance during the transmittance measurements.

Disclosures. The authors declare no conflict of interests.

Data availability. Data underlying the results presented in this paper are not publicly available at this time but may be obtained from the authors upon reasonable request.

References

1. M. Stegmaier, C. Ríos, H. Bhaskaran, C. D. Wright, and W. H. P. Pernice, "Nonvolatile all-optical 1 × 2 switch for chipscale photonic networks," Adv. Opt. Mater. **5**, 1600346 (2017).
2. C. Ríos, M. Stegmaier, P. Hosseini, D. Wang, T. Scherer, C. D. Wright, H. Bhaskaran, and W. H. P. Pernice, "Integrated all-photonic non-volatile multi-level memory," Nat. Photonics **9**, 725–732 (2015).
3. W. H. P. Pernice and H. Bhaskaran, "Photonic non-volatile memories using phase change materials," Appl. Phys. Lett. **101**, 171101 (2012).
4. J. Feldmann, N. Youngblood, C. D. Wright, H. Bhaskaran, and W. H. P. Pernice, "All-optical spiking neurosynaptic networks with self-learning capabilities," Nature **569**, 208–214 (2019).
5. S. Abdollahramezani, O. Hemmatyar, H. Taghinejad, A. Krasnok, Y. Kiarashinejad, M. Zandehshahvar, A. Alu, and A. Adibi, "Tunable nanophotonics enabled by chalcogenide phase-change materials," Nanophotonics **9**, 1189–1241 (2020).
6. S. Cueff, A. Taute, A. Bourgade, J. Lumeau, S. Monfray, Q. Song, P. Genevet, B. Devif, X. Letartre, and L. Berguiga, "Reconfigurable flat optics with programmable reflection amplitude using lithography-free phase-change material ultra-thin films," Adv. Opt. Mater. **9**, 2170006 (2021).
7. W. Dong, H. Liu, J. K. Behera, L. Lu, R. J. H. Ng, K. V. Sreekanth, X. Zhou, J. K. W. Yang, and R. E. Simpson, "Wide bandgap phase change material tuned visible photonics," Adv. Funct. Mater. **29**, 1806181 (2019).
8. C. Chen, D. C. Bobela, Y. Yang, S. Lu, K. Zeng, C. Ge, B. Yang, L. Gao, Y. Zhao, M. C. Beard, and J. Tang, "Characterization of basic physical properties of Sb_2Se_3 and its relevance for photovoltaics," Front. Optoelectron. **10**, 18–30 (2017).

Optical Materials EXPRESS

9. N. Yamada, E. Ohno, K. Nishiuchi, N. Akahira, and M. Takao, "Rapid-phase transitions of GeTe-Sb_2Te_3 pseudobinary amorphous thin films for an optical disk memory," J. Appl. Phys. **69**, 2849–2856 (1991).
10. G. Mirabelli, C. McGeough, M. Schmidt, E. K. McCarthy, S. Monaghan, I. M. Povey, M. McCarthy, F. Gity, R. Nagle, G. Hughes, A. Cafolla, P. K. Hurley, and R. Duffy, "Air sensitivity of MoS_2, $MoSe_2$, $MoTe_2$, HfS_2, and $HfSe_2$," J. Appl. Phys. **120**, 125102 (2016).
11. M. Delaney, I. Zeimpekis, D. Lawson, D. W. Hewak, and O. L. Muskens, "A new family of ultralow loss reversible phase-change materials for photonic integrated circuits: Sb_2S_3 and Sb_2 Se_3," Adv. Funct. Mater. **30**, 2002447 (2020).
12. E. P. T. Tyndall, "Optical properties of some metallic sulfides," Phys. Rev. **21**, 162–180 (1923).
13. P. Drude, "Beobachtungen über die Reflexion des Lichtes am Antimonglanz," Ann. Phys. (Berlin, Ger.) **270**, 489–531 (1888).
14. M. Schubert, T. Hofmann, C. M. Herzinger, and W. Dollase, "Generalized ellipsometry for orthorhombic, absorbing materials: dielectric functions, phonon modes and band-to-band transitions of Sb_2S3," Thin Solid Films **455**, 619–623 (2004).
15. M. Schubert and W. Dollase, "Generalized ellipsometry for biaxial absorbing materials: determination of crystal orientation and optical constants of Sb_2S_3," Opt. Lett. **27**, 2073 (2002).
16. S. Funke, M. Duwe, F. Balzer, P. H. Thiesen, K. Hingerl, and M. Schiek, "Determining the dielectric tensor of microtextured organic thin films by imaging Mueller matrix ellipsometry," J. Phys. Chem. Lett. **12**, 3053–3058 (2021).
17. C. Cobianu, M. Gheorghe, M. Modreanu, Y. Gutierrez, and M. Losurdo, "Chemically bath deposited Sb_2S_3 films as optical phase change materials," in *2021 International Semiconductor Conference (CAS)* (IEEE, 2021), pp. 249–252.
18. G. E. Jellison and F. A. Modine, "Parameterization of the optical functions of amorphous materials in the interband region," Appl. Phys. Lett. **69**, 371–373 (1996).
19. R. M. A. Azzam, "Photopolarimetric measurement of the Mueller matrix by Fourier analysis of a single detected signal," Opt. Lett. **2**, 148 (1978).
20. O. Arteaga and B. Kahr, "Characterization of homogenous depolarizing media based on Mueller matrix differential decomposition," Opt. Lett. **38**, 1134 (2013).
21. R. M. A. Azzam, "Propagation of partially polarized light through anisotropic media with or without depolarization: a differential 4×4 matrix calculus," J. Opt. Soc. Am. **68**, 1756 (1978).
22. R. Ossikovski, "Differential matrix formalism for depolarizing anisotropic media," Opt. Lett. **36**, 2330 (2011).
23. J. J. Gil Pérez and R. Ossikovski, *Polarized Light and the Mueller Matrix Approach* (CRC Press, 2017).
24. M. I. Medina-Montes, Z. Montiel-González, F. Paraguay-Delgado, N. R. Mathews, and X. Mathew, "Structural, morphological and spectroscopic ellipsometry studies on sputter deposited Sb_2S_3 thin films," J. Mater. Sci. Mater. Electron. **27**, 9710–9719 (2016).
25. R. Parize, T. Cossuet, O. Chaix-Pluchery, H. Roussel, E. Appert, and V. Consonni, "In situ analysis of the crystallization process of Sb_2S_3 thin films by Raman scattering and X-ray diffraction," Mater. Des. **121**, 1–10 (2017).
26. C. L. Hassam, F. Sciortino, N. T. K. Nguyen, B. Srinivasan, K. Ariga, F. Gascoin, F. Grasset, T. Mori, T. Uchikoshi, Y. Thimont, and D. Berthebaud, "Robust, transparent hybrid thin films of phase-change material Sb_2S_3 prepared by electrophoretic deposition," ACS Appl. Energy Mater. **4**, 9891–9901 (2021).
27. B. Crist and J. M. Schultz, "Polymer spherulites: a critical review," Prog. Polym. Sci. **56**, 1–63 (2016).
28. A. G. Shtukenberg, Y. O. Punin, E. Gunn, and B. Kahr, "Spherulites," Chem. Rev. **112**, 1805–1838 (2012).
29. I. E. Bolotov, A. V. Kozhin, and S. B. Fishelav, "Crystallization of thin films of antimony sulfide," Sov. Phys. J. **13**, 1655–1657 (1970).
30. A. A. Sokol, V. M. Kosevich, and A. G. Bagmut, "Defect structure of Sb_2S_3 crystals revealed by electron microscope crystal lattice imaging techniques," in *Growth of Crystals* (Springer US, 1986), pp. 322–331.
31. W. Cui, M. Li, Z. Dai, Q. Meng, and Y. Zhu, "Near-field optical effect of a core-shell nanostructure in proximity to a flat surface," J. Chem. Phys. **140**, 1 (2014).
32. X. Cui, S. M. Nichols, O. Arteaga, J. Freudenthal, F. Paula, A. G. Shtukenberg, and B. Kahr, "Dichroism in helicoidal crystals," J. Am. Chem. Soc. **138**, 12211–12218 (2016).
33. H. M. Ye, J. H. Freudenthal, M. Tan, J. Yang, and B. Kahr, "Chiroptical differentiation of twisted chiral and achiral polymer crystals," Macromolecules **52**, 8514–8520 (2019).
34. B. Dörling, A. Sánchez-Díaz, O. Arteaga, A. Veciana, M. I. Alonso, and M. Campoy-Quiles, "Controlled pinning of conjugated polymer spherulites and its application in detectors," Adv. Opt. Mater. **5**, 1–10 (2017).

143.239.45.11 {ts '2022-03-21 08:26:07'}